

# Machine-learning-accelerated Bose-Einstein condensation

Zachary Vendeiro, Joshua Ramette, Alyssa Rudelis, Michelle Chong,

Josiah Sinclair, Luke Stewart, Alban Urvoy,\* and Vladan Vuletić†

*Department of Physics, MIT-Harvard Center for Ultracold Atoms and Research Laboratory of Electronics,  
Massachusetts Institute of Technology, Cambridge, Massachusetts 02139, USA*

(Dated: May 18, 2022)

Machine learning is emerging as a technology that can enhance physics experiment execution and data analysis. Here, we apply machine learning to accelerate the production of a Bose-Einstein Condensate (BEC) of  $^{87}\text{Rb}$  atoms by Bayesian optimization of up to 55 control parameters. This approach enables us to prepare BECs of  $2.8 \times 10^3$  optically trapped  $^{87}\text{Rb}$  atoms from a room-temperature gas in 575 ms. The algorithm achieves the fast BEC preparation by applying highly efficient Raman cooling to near quantum degeneracy, followed by a brief final evaporation. We anticipate that many other physics experiments with complex nonlinear system dynamics can be significantly enhanced by a similar machine-learning approach.

Recently, researchers have begun applying machine learning techniques to atomic physics experiments, e.g., to enhance data processing for imaging [1–5], determine the ground state and dynamics of many-body systems [6, 7], or to identify phases and phase transitions [8–10]. One promising practical application of machine learning to atomic physics is in the optimization of control sequences with many parameters and nonlinear dynamics [11–16], and in particular to one of the workhorses of atomic physics, Bose-Einstein condensates (BECs) [11, 13–16].

With few exceptions [17], experiments on BECs end with a destructive measurement, which requires repeated BEC preparation. Approaches to increase the BEC production rate, and associated signal-to-noise ratio of the experiments, have generally relied heavily on hardware improvements [18–22], or used atomic species with narrower optical transitions [18, 21, 22] than offered by the most widely utilized alkali atoms. For alkali atoms, the tight confinement of atom-chip magnetic traps has enabled fast evaporation sequences, with a complex multi-layer atom-chip achieving BEC preparation times of 850 ms for  $4 \times 10^4$  atoms [19]. Non-alkali atoms featuring narrow optical transitions can be used to reach lower temperatures in narrow-line MOTs [18, 21, 22]. That approach, combined with a dynamically tunable optical dipole trap, has recently been used to prepare BECs of  $2 \times 10^4$  erbium atoms in under 700 ms [22].

In this Letter, we demonstrate a complementary approach where, in a simple experimental setup with a single MOT and a standard alkali atom, machine learning is leveraged to optimize a complex nonlinear laser and evaporative cooling process to quantum degeneracy. Controlling a sequence with up to 55 interdependent experimental parameters, Bayesian optimization [11, 12, 23], a technique commonly used in machine learning, finds parameter values which cool a gas from room temperature into the quantum degenerate regime in 575 ms, creating a BEC containing  $N_{\text{BEC}} = 2.8 \times 10^3$  atoms. To our knowledge, this is the fastest BEC creation to date. We

further find that the choice of cost function for the algorithm strongly influences the trade-off between final atom number and the purity of the created BEC.

Our apparatus employs only a single MOT directly loaded from a  $^{87}\text{Rb}$  background vapor, a crossed optical dipole trap, and two Raman cooling beams as depicted in Fig. 1(a). No Zeeman slower, two-dimensional MOT, atom chip [19], dynamic trap shaping [21], or strobing [22, 24] are necessary. Using Raman cooling in a crossed optical dipole trap (cODT), a method that can reach very high phase-space density and even condensation [25], the algorithm also achieves a cooling slope of 16 orders of magnitude improvement in phase space density (PSD) per order of magnitude in atom loss ( $\gamma = 16$ ) up to the threshold to quantum degeneracy. This is significantly better than the  $\gamma = 7.2$  value we could obtain with extensive manual optimization under similar conditions [25]. The algorithm autonomously discovered grey molasses [26, 27] during trap loading, which is superior to standard polarization gradient cooling at high atomic densities. Remarkably, the algorithm learns to turn off the Raman cooling at the threshold to condensation, and employ a final short evaporation to create almost pure condensates.

The Raman cooling implementation used in this work is similar to that of Ref. [25]. Cooling proceeds in a cODT formed by intersecting two non-interfering 1064 nm beams, one horizontal and one vertical, as shown in Fig. 1(a). Two 795-nm beams drive the Raman cooling: the optical pumping beam and the Raman coupling beam. Both beams are large enough to address atoms along the length of the horizontal ODT. Raman cooling [28] provides sub-Doppler cooling by driving velocity-selective Raman transitions between hyperfine states, here the  $|F = 2, m_F = -2\rangle$  and  $|2, -1\rangle$  states of  $^{87}\text{Rb}$  [25]. The Raman transitions are non-dissipative so entropy is removed from the atomic gas in the form of spontaneously scattered photons as atoms are optically pumped back to the dark state  $|2, -2\rangle$ . Light-assisted collisions, which typically prohibit laser cooling

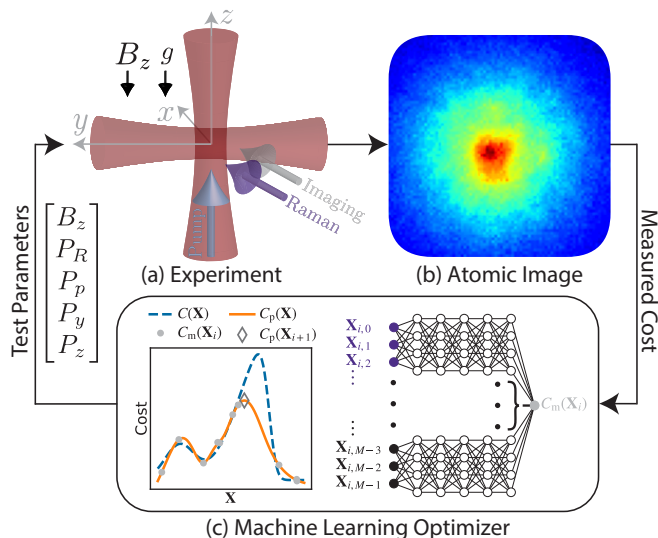


FIG. 1. (a) Beam setup showing 1064-nm horizontal (waist  $w_h = 18 \mu\text{m}$ ) and vertical ( $w_v = 14 \mu\text{m}$ ) optical-trapping beams, 795 nm Raman coupling ( $w_R = 500 \mu\text{m}$ ) and optical pumping (elliptical profile with  $w_x = 30 \mu\text{m}$  along  $x$  and  $w_y \sim 1 \text{ mm}$  waist along  $y$ ) beams, and 780-nm absorption-imaging beam. (b) Typical absorption image acquired to extract the cost function value for a set of parameter values  $\mathbf{X}$ . (c) Bayesian optimization is based on developing a model, here a neural network. The model  $C_p(\mathbf{X})$  (orange solid line) attempts to predict the actual system performance  $C(\mathbf{X})$  (blue dashed line). The model is trained on all measured results  $C_m(\mathbf{X}_i)$  (light gray circles), which generally include noise. The algorithm uses the model to predict optimal parameter values  $\mathbf{X}_{i+1}$  (open gray diamond), then tests those values. The model is updated using the newly measured results, then a new iteration begins with the improved model. In (c),  $\mathbf{X}$  is depicted as a single parameter, while in reality it is a vector with an entry for each of the  $M$  optimization parameters shown as inputs to the neural network.

at high atomic densities, are suppressed by detuning the optical pumping light 4.33 GHz to the red of the  $D_1$   $F = 2 \rightarrow F' = 2'$  transition, where a local minimum of light-induced loss was observed [25]. For simplicity, the far-detuned optical-pumping beam is also used to drive one of the legs of the Raman transitions.

The Raman cooling dynamics are controlled via five actuators: (i) the horizontal  $P_y$  and (ii) vertical  $P_z$  trap beam powers which set the trap depth and frequencies, (iii) the power  $P_p$  of the optical pumping beam which sets the optical-pumping rate, (iv) the Raman coupling beam power  $P_R$  which tunes the Raman coupling Rabi frequency, and (v) the magnetic field  $B_z$  which adjusts the resonant velocity class for the Raman transition. The cooling procedure is divided into stages during which the controls are linearly ramped, with the endpoints of each ramp constituting the optimization parameters.

The optimization problem can be formulated as the maximization of a cost function  $C$ , which is a mapping

from sets of parameter values  $\mathbf{X} \in \mathbb{R}^M$  to a corresponding cost value  $C(\mathbf{X}) \in \mathbb{R}$ , where  $M$  is the number of optimization parameters. The cost  $C$  quantifies the quality of the results produced by the set of parameter values, and is generally a priori unknown, but can be extracted from measurements. Bayesian optimization is well-suited for this type of problem as it can tolerate noise in the measured cost and typically requires testing fewer values of  $\mathbf{X}$  than other optimization methods [11–16].

Bayesian optimization begins with collecting a training dataset by experimentally measuring the cost  $C_m(\mathbf{X}_i)$  for various values of sets of parameter values  $\mathbf{X}_i$ . The  $\mathbf{X}_i$  used to construct the training dataset are chosen by a training algorithm, which can implement another optimization algorithm or can select  $\mathbf{X}_i$  randomly. A model of the cost function is then fit to the training dataset which approximates the unknown true cost function  $C(\mathbf{X})$ . Although Bayesian optimization typically uses a Gaussian process for its model [23], the present work uses neural networks [12, 29], as depicted in Fig. 1(c). Neural networks were chosen for their significantly faster fitting time for our typical number of optimization parameters. Once the model is fit, a standard numerical optimization algorithm is applied to the modeled cost function  $C_p(\mathbf{X})$  to determine which value  $\mathbf{X}_{i+1}$  for the next iteration is predicted to yield the best cost, as depicted in Fig. 1(c). Optionally this numerical optimization can be constrained to a trust region, which is a smaller volume of parameter space, centered around the  $\mathbf{X}_i$  which yielded the best cost measured thus far. The predicted optimal value  $\mathbf{X}_{i+1}$  is then tested by experimentally measuring the corresponding cost  $C_m(\mathbf{X}_{i+1})$ . The next iteration begins by retraining the model with the new result, and making a new prediction for the optimal value of  $\mathbf{X}$  with the updated model. To encourage parameter-space exploration, additional iterations of the training algorithm can be run periodically, and those results are incorporated into the model as well. The algorithm iterates until it reaches a termination criterion, such as a set maximum number of iterations, or a set number of consecutive iterations that fail to return better results.

Since the optimization transitions the gas from the classical into the quantum degenerate regime, the final state of the gas depends strongly on how the cost function is chosen as a combination of the experimentally measured parameters atom number  $N$  and temperature  $T$ . The classical phase space density  $\text{PSD}_c$  is defined as  $n_c \lambda_{\text{dB}}^3$ , where  $\lambda_{\text{dB}}$  is the thermal de Broglie wavelength and  $n_c$  is the calculated peak number density neglecting boson statistics. The value of  $\text{PSD}_c$  is nearly equal to the true PSD when  $\text{PSD} \ll 1$ , while at the threshold to condensation,  $\text{PSD}_c \sim 1$ . (See [30] for details on the calculation of  $\text{PSD}_c$ .) Since the temperature  $T$  is more difficult to determine in the quantum degenerate regime, and also requires a fit to the data with potential convergence problems, we instead measure  $N$  and the peak

optical depth OD in an absorption image taken after 1.5 to 8 ms of time-of-flight expansion. (To compare different sequences on an equal footing, the trap beams are always ramped to a fixed power setting before releasing the atoms for time-of-flight imaging.) Generally ensembles with larger  $\text{PSD}_c$  have a larger atom number  $N$  and less expansion energy, which leads to a larger peak optical depth OD for a given  $N$ . Guided by this, we explored cost functions of the form

$$C(\mathbf{X}) \propto f(N)\text{OD}^3 N^{\alpha-9/5} \quad (1)$$

with  $f(N) = 2/(1 + e^{N_1/N})$  for  $N > 0$  and  $f(N) = 0$  for  $N \leq 0$ . The function  $f(N)$ , with  $N_1$  being a threshold atom number chosen near the noise floor of the atom number measurement, is introduced to prevent the cost from diverging as  $N$  approaches zero, while having little effect otherwise.

The parameter  $\alpha$  in the cost function tunes the trade-off between optimizing for larger atom number or lower temperature. Larger  $\alpha$  puts more emphasis on increasing  $N$ , while lower  $\alpha$  favors lower  $T$ . For a pure BEC after sufficient time-of-flight expansion,  $C/f$  scales as  $(N_{\text{BEC}})^\alpha$  (see SM [30]). For a purely thermal cloud,  $C/f$  is proportional to  $\text{PSD}_c$  when  $\alpha = -1/5$ , though that value of  $\alpha$  is unsuitable for condensed clouds as the cost then scales inversely with  $N$ .

All optimization was performed with the open-source packages M-LOOP [11, 12] to implement the Bayesian optimization and Labscript [31] for experimental control. The sequence begins with a separately optimized 99-ms long MOT loading and compression period. Notably, the algorithm discovered grey molasses [26, 27], which it applies at the end of the compression sequence. This outperforms the bright molasses [32, 33] that was previously used in the manually-optimized compression sequence, with the grey molasses loading a similar number of atoms in one tenth of the time. The trap beam powers are ramped to their initial Raman cooling values during the last 10 ms of the MOT compression and then the magnetic field is adjusted to its initial Raman cooling value in 1 ms, at which point the horizontal dipole trap holds typically  $N = 2.7 \times 10^5$  atoms.

We then added 100-ms stages of Raman cooling one by one and optimized them individually. After five stages, the algorithm tended to turn off the Raman cooling by turning down  $P_p$  or  $P_R$  or by tuning the magnetic field  $B_z$  such that the Raman transition became off-resonant. This likely occurred because the cloud temperature  $T$  was below the effective recoil temperature [25] where Raman cooling, even with optimal parameters, becomes too slow, while leading to trap loss and heating due to light-assisted collisions [34]. The Bayesian model recognized this and shut down the Raman cooling at this point, with the atomic gas close to condensation. We then added up to six shorter 30-ms long stages in which the optical pumping and Raman coupling beams were turned

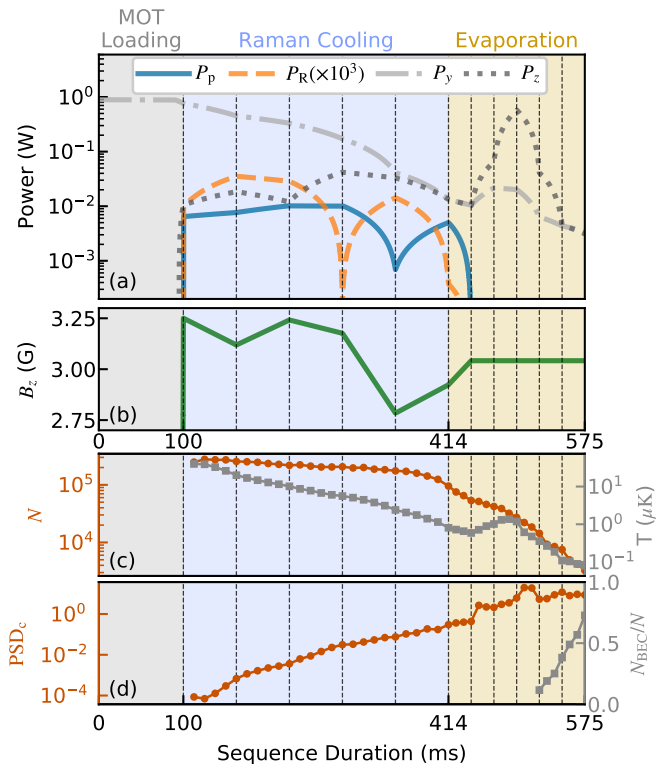


FIG. 2. The control waveforms (a-b) and measured atomic-gas properties (c-d) of the optimized sequence. Gray, blue and orange shadings mark the MOT loading period, the Raman cooling period, and the evaporation periods, respectively. The Raman coupling beam power has been multiplied by  $10^3$  for better visibility. The value of  $\text{PSD}_c$  does not account for bosonic statistics and thus remains relatively flat across the BEC transition, however the condensate fraction quickly increases after the BEC threshold is crossed.

off, and the algorithm performed evaporative cooling by reducing the trap powers. Due to the reduced number of parameters, we were able to optimize the evaporation stages simultaneously, which produced a BEC. Subsequently we shortened the Raman cooling and evaporation stages with parameter values fixed until only a small and impure BEC was produced, and then ran a global reoptimization. In this global optimization stage, all 42 of the Raman cooling and evaporation parameters were reoptimized simultaneously using the previous values as the initial guess for  $\mathbf{X}$ . We repeated this shortening of the cooling sequence and reoptimization procedure until the optimization failed to find parameters that could produce sufficiently pure BECs.

The required beam powers generally varied over several orders of magnitude, so the logarithm of their powers were used as entries in  $\mathbf{X}$ , while the magnetic-field control parameter  $B_z$  was kept a linear parameter. A feedforward adjustment was included in the  $B_z$  control values to account for the light shift of the  $|2, -1\rangle$  state by the optical pumping beam. We averaged over five

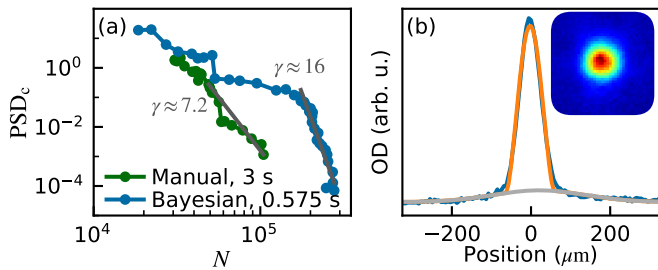


FIG. 3. Results of the 575 ms optimized sequence. (a) Parametric plot of  $\text{PSD}_c$  as a function of  $N$  until the appearance of a BEC. A fit (gray line) to the early part of the sequence shows that the initial cooling up to  $\text{PSD}_c \sim 10^{-1}$  occurs with  $\gamma \approx 16$ , significantly more efficient than is achievable with evaporative cooling. The results from the manually-optimized and much slower (3 s-long) sequence of Ref. [25] are also shown for comparison, which proceeds with  $\gamma \approx 7.2$  initially. (b) The horizontal cross section of the resulting atomic gas after a 24 ms time-of-flight expansion, averaged over 200 repetitions, clearly indicating a large BEC population and small thermal wings. The inset shows the 2D absorption image of the cloud.

repetitions of the experiment for each set of parameter values tested, which took  $\sim 10$  s accounting for experimental and analysis overhead. The analysis for each iteration typically took longer than the time required to perform the experiment, so two independent optimizations were generally run on different computers in parallel for maximal machine time usage. The number of iterations per optimization varied but typically involved  $\sim 1000$  iterations (including the initial training), and ran for several hours, both for the single-stage optimizations and the full-sequence optimizations. A simpler optimization procedure was also attempted which did not involve optimizations of individual stages. Instead the sequence was divided into ten 100 ms stages and all 55 parameters were optimized from scratch simultaneously. That approach combined with the shortening and reoptimizing procedure successfully produced a similar BEC, albeit in slightly longer time (650 ms vs 575 ms), possibly due to the optimization becoming trapped in a local optimum.

The best discovered 575-ms long control sequence is depicted in Fig. 2(a-b), and the corresponding results are depicted in Fig. 2(c-d) and Fig. 3. After the MOT loading stage and transfer into the cODT, five  $\sim 63$ -ms long stages of Raman cooling follow, and then the optical pumping and Raman beams are ramped off, followed by six  $\sim 27$ -ms long evaporation stages. As observed in previous work [12–14], the ramps produced by Bayesian optimization are non-monotonic and non-intuitive, but they outperform the monotonic routines we found by manual optimization.

The BEC is fully prepared at the end of the evaporation stages, 575 ms after the start of the MOT loading. The final cloud contains  $3.7 \times 10^3$  total atoms and is

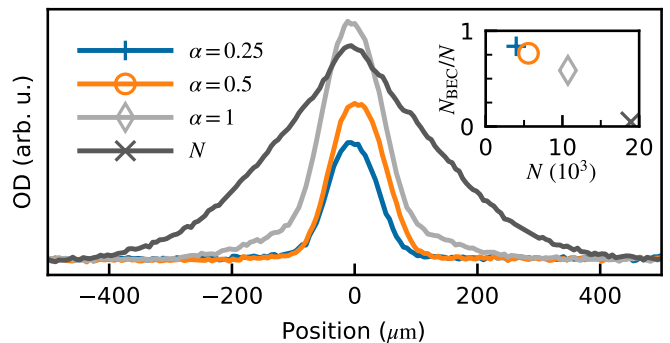


FIG. 4. Cross sections of atomic clouds optimized for different cost function parameter  $\alpha$  (see main text) with a 1 s long sequence, demonstrating the trade off between optimizing for atom number or temperature. Also plotted are the results of optimizing only for total atom number  $N$ . For fair comparison, images are taken after release from fixed trap beam power settings. Each cross section is the average of 200 images, taken after a 24 ms of time-of-flight expansion. Inset: Condensate fraction  $N_{\text{BEC}}/N$  plotted against  $N$ .

shown in Fig. 3(b). A bimodal fit of the cloud indicates that  $2.8 \times 10^3$  atoms (76 %) are in the BEC. Although the sequence was optimized for speed rather than efficiency, the initial cooling occurs with a logarithmic slope  $\gamma = d(\log \text{PSD}_c)/d(\log N) \approx 16$ .

The atomic gases produced by sequences optimized for different values of  $\alpha$  are presented in Fig. 4, as well as the results when optimizing for total atom number ( $N$ ). These optimizations were performed with a sequence duration of 1 s to ensure ample cooling time, and  $N_1$  was set to  $1.2 \times 10^3$ . Larger values of  $\alpha$  result in more atoms, but at higher temperature and lower condensate fraction. Smaller values of  $\alpha$  produce purer BECs, but with fewer atoms overall. Setting  $\alpha$  to 0.5 was found to make a reasonable compromise (orange curve in Fig. 4); so that value was used for the final full-sequence optimization which yielded the sequence presented in Fig. 2.

In conclusion, we have demonstrated that Raman cooling with far detuned optical-pumping light combined with a final evaporation can rapidly produce BECs with a comparatively simple apparatus, even with a standard alkali atom which lacks narrow optical transitions. Bayesian optimization greatly eased the search for a short sequence to BEC, quickly discovering unintuitive yet high-performing sequences that are unlikely to be found manually. In future applications, user intervention may be further reduced by including the sequence duration as an additional optimization parameter and factoring the sequence length into the assigned cost [14]. The methods demonstrated in this work are generalizable to other species, and can likely be added to new or existing experiments without extensive effort. We anticipate that many other experimental procedures in atomic physics and beyond can be improved by machine learning.

The authors would like to thank Martin Zwiernik for inspiring discussions and loan of a 1064 nm fiber amplifier. They would also like to thank Michael Hush, Harry Slatyer, Philip Starkey, Christopher Billington, and Russell Anderson for stimulating discussions and software assistance. This work was in part supported by the NSF, NSF CUA, NASA, DoE, and MURI through ONR.

---

\* Current affiliation: Laboratoire Kastler Brossel, Sorbonne Université, CNRS, ENS-Université PSL, Collège de France, 4 place Jussieu, 75005 Paris, France

† vuletic@mit.edu

- [1] L. R. Picard, M. J. Mark, F. Ferlaino, and R. van Bijnen, Deep learning-assisted classification of site-resolved quantum gas microscope images, *Measurement Science and Technology* **31**, 025201 (2019).
- [2] Z.-H. Ding, J.-M. Cui, Y.-F. Huang, C.-F. Li, T. Tu, and G.-C. Guo, Fast high-fidelity readout of a single trapped-ion qubit via machine-learning methods, *Physical Review Applied* **12**, 014038 (2019).
- [3] A. Seif, K. A. Landsman, N. M. Linke, C. Figgatt, C. Monroe, and M. Hafezi, Machine learning assisted readout of trapped-ion qubits, *Journal of Physics B: Atomic, Molecular and Optical Physics* **51**, 174006 (2018).
- [4] G. Ness, A. Vainbaum, C. Shkedrov, Y. Florshaim, and Y. Sagi, Single-exposure absorption imaging of ultracold atoms using deep learning, *Physical Review Applied* **14**, 014011 (2020).
- [5] S. Guo, A. R. Fritsch, C. Greenberg, I. Spielman, and J. P. Zolot, Machine-learning enhanced dark soliton detection in Bose-Einstein condensates, *Machine Learning: Science and Technology* **2**, 035020 (2021).
- [6] G. Carleo and M. Troyer, Solving the quantum many-body problem with artificial neural networks, *Science* **355**, 602 (2017).
- [7] H. Saito, Solving the Bose-Hubbard model with machine learning, *Journal of the Physical Society of Japan* **86**, 093001 (2017).
- [8] L. Wang, Discovering phase transitions with unsupervised learning, *Physical Review B* **94**, 195105 (2016).
- [9] J. Carrasquilla and R. G. Melko, Machine learning phases of matter, *Nature Physics* **13**, 431 (2017).
- [10] G. Torlai, B. Timar, E. P. L. van Nieuwenburg, H. Levine, A. Omran, A. Keesling, H. Bernien, M. Greiner, V. Vuletić, M. D. Lukin, R. G. Melko, and M. Endres, Integrating neural networks with a quantum simulator for state reconstruction, *Phys. Rev. Lett.* **123**, 230504 (2019).
- [11] P. B. Wigley, P. J. Everitt, A. van den Hengel, J. W. Bastian, M. A. Sooriyabandara, G. D. McDonald, K. S. Hardman, C. D. Quinlivan, P. Manju, C. C. Kuhn, *et al.*, Fast machine-learning online optimization of ultra-cold-atom experiments, *Scientific reports* **6**, 1 (2016).
- [12] A. D. Tranter, H. J. Slatyer, M. R. Hush, A. C. Leung, J. L. Everett, K. V. Paul, P. Vernaz-Gris, P. K. Lam, B. C. Buchler, and G. T. Campbell, Multiparameter optimisation of a magneto-optical trap using deep learning, *Nature communications* **9**, 1 (2018).
- [13] I. Nakamura, A. Kanemura, T. Nakaso, R. Yamamoto, and T. Fukuhara, Non-standard trajectories found by machine learning for evaporative cooling of 87 Rb atoms, *Optics express* **27**, 20435 (2019).
- [14] A. J. Barker, H. Style, K. Luksch, S. Sunami, D. Garrick, F. Hill, C. J. Foot, and E. Bentine, Applying machine learning optimization methods to the production of a quantum gas, *Machine Learning: Science and Technology* **1**, 015007 (2020).
- [15] E. Davletov, V. Tsyganok, V. Khlebnikov, D. Pershin, D. Shaykin, and A. Akimov, Machine learning for achieving Bose-Einstein condensation of thulium atoms, *Physical Review A* **102**, 011302 (2020).
- [16] Y. Wu, Z. Meng, K. Wen, C. Mi, J. Zhang, and H. Zhai, Active learning approach to optimization of experimental control, *Chinese Physics Letters* **37**, 103201 (2020).
- [17] C.-C. Chen, R. G. Escudero, J. Minář, B. Pasquiou, S. Bennetts, and F. Schreck, Continuous Bose-Einstein condensation, arXiv preprint arXiv:2012.07605 (2021).
- [18] S. Stellmer, R. Grimm, and F. Schreck, Production of quantum-degenerate strontium gases, *Phys. Rev. A* **87**, 013611 (2013).
- [19] J. Rudolph, W. Herr, C. Grzeschik, T. Sterneke, A. Grote, M. Popp, D. Becker, H. Müntinga, H. Ahlers, A. Peters, *et al.*, A high-flux beam source for mobile atom interferometers, *New Journal of Physics* **17**, 065001 (2015).
- [20] C.-L. Hung, X. Zhang, N. Gemelke, and C. Chin, Accelerating evaporative cooling of atoms into Bose-Einstein condensation in optical traps, *Physical Review A* **78**, 011604 (2008).
- [21] R. Roy, A. Green, R. Bowler, and S. Gupta, Rapid cooling to quantum degeneracy in dynamically shaped atom traps, *Physical Review A* **93**, 043403 (2016).
- [22] G. A. Phelps, A. Hébert, A. Krahn, S. Dickerson, F. Öztürk, S. Ebadi, L. Su, and M. Greiner, Sub-second production of a quantum degenerate gas, arXiv preprint arXiv:2007.10807 (2020).
- [23] B. Shahriari, K. Swersky, Z. Wang, R. P. Adams, and N. De Freitas, Taking the human out of the loop: A review of Bayesian optimization, *Proceedings of the IEEE* **104**, 148 (2015).
- [24] N. R. Hutzler, L. R. Liu, Y. Yu, and K.-K. Ni, Eliminating light shifts for single atom trapping, *New Journal of Physics* **19**, 023007 (2017).
- [25] A. Urvoy, Z. Vendeiro, J. Ramette, A. Adiyatullin, and V. Vuletić, Direct laser cooling to Bose-Einstein condensation in a dipole trap, *Phys. Rev. Lett.* **122**, 203202 (2019).
- [26] M. Weidemüller, T. Esslinger, M. A. Ol'shanii, A. Hemmerich, and T. W. Hänsch, A novel scheme for efficient cooling below the photon recoil limit, *EPL (Europhysics Letters)* **27**, 109 (1994).
- [27] D. Boiron, C. Triché, D. Meacher, P. Verkerk, and G. Grynberg, Three-dimensional cooling of cesium atoms in four-beam gray optical molasses, *Physical Review A* **52**, R3425 (1995).
- [28] M. Kasevich and S. Chu, Laser cooling below a photon recoil with three-level atoms, *Physical Review Letters* **69**, 1741 (1992).
- [29] J. Snoek, O. Rippel, K. Swersky, R. Kiros, N. Satish, N. Sundaram, M. M. A. Patwary, Prabhat, and R. P. Adams, Scalable bayesian optimization using deep neural networks (2015), arXiv:1502.05700 [stat.ML].

- [30] See Supplemental Material at [*URL will be inserted by publisher*], which includes Ref. [35], for details on the calculation of  $\text{PSD}_c$ , derivation of cost function scalings, and details on the Raman cooling laser requirements.
- [31] P. T. Starkey, C. J. Billington, S. P. Johnstone, M. Jasperse, K. Helmerson, L. D. Turner, and R. P. Anderson, A scripted control system for autonomous hardware-timed experiments, *Review of Scientific Instruments* **84**, 085111 (2013).
- [32] P. D. Lett, R. N. Watts, C. I. Westbrook, W. D. Phillips, P. L. Gould, and H. J. Metcalf, Observation of atoms laser cooled below the Doppler limit, *Physical review letters* **61**, 169 (1988).
- [33] J. Dalibard and C. Cohen-Tannoudji, Laser cooling below the Doppler limit by polarization gradients: simple theoretical models, *JOSA B* **6**, 2023 (1989).
- [34] K. Burnett, P. S. Julienne, and K.-A. Suominen, Laser-Driven Collisions between Atoms in a Bose-Einstein Condensed Gas, *Physical Review Letters* **77**, 1416 (1996).
- [35] F. Dalfovo, S. Giorgini, L. P. Pitaevskii, and S. Stringari, Theory of Bose-Einstein condensation in trapped gases, *Reviews of Modern Physics* **71**, 463 (1999).

## Supplemental Materials: Machine-learning-accelerated Bose-Einstein condensation

### CLASSICAL PHASE SPACE DENSITY CALCULATION

The classical phase space density is defined as  $\text{PSD}_c = n_c \lambda_{\text{dB}}^3$  where  $n_c$  is the peak number density calculated for a classical gas (i.e. neglecting Bosonic statistics) and  $\lambda_{\text{dB}} = h/\sqrt{2\pi m k_B T}$  is the de Broglie wavelength. Here  $h$  is the Planck constant,  $m$  is the mass of an atom, and  $k_B$  is the Boltzmann constant. To calculate  $\text{PSD}_c$  for a cloud, its atom number  $N$  and temperature  $T$  are measured and it is assumed to be in thermal equilibrium. The value of  $\lambda_{\text{dB}}$  is easily calculated from the measured temperature. The partition function  $Z = \int f(\mathbf{x}) dV$  is then calculated by numerically integrating the Boltzmann factor  $f(\mathbf{x}) = \exp[-U(\mathbf{x})/(k_B T)]$  over the trap volume, where  $U(\mathbf{x})$  is the trap potential at position  $\mathbf{x}$ . The  $U(\mathbf{x})$  is taken to be the sum of two Gaussian beams, one for each cODT beam, and gravity is neglected for simplicity. Each Gaussian beam with peak depth  $U_{i,0}$  and waist  $w_{i,0}$  contributes a potential of the form

$$U_i(\mathbf{x}) = U_{i,0} \left( \frac{w_{i,0}}{w_i(z')} \right)^2 \exp \left( \frac{-2(r')^2}{w_i(z')^2} \right) \quad (\text{S1})$$

where  $w_i(z') = w_{i,0} \sqrt{1 + (z'/z_R)^2}$  is the spatially-varying beam width and  $z_R = \pi w_{i,0}^2/\lambda$  is the Rayleigh range. The primed coordinates  $z'$  and  $r'$  are taken to be along and perpendicular to the beam's propagation direction respectively. The value of  $n_c$  can be calculated as  $Nf(\mathbf{x}_0)/Z$  where  $\mathbf{x}_0$  is the position of the bottom of the trap. Finally  $\text{PSD}_c$  is evaluated from its definition in terms of  $n_c$  and  $\lambda_{\text{dB}}$ . Notably, for much of the sequence the atomic cloud extends out of the cODT region and into the wings of the horizontal ODT, in which case the trap potential seen by the cloud is not harmonic. Thus the well-known result  $\text{PSD}_c = N(\hbar\bar{\omega})^3/(k_B T)^3$  for a harmonic trap with geometric mean trap frequency  $\bar{\omega}$  cannot be used for most of the sequence.

The above calculation assumes that the cloud is in thermal equilibrium, which is often a good approximation. However, after about 440 ms of the final optimized 575 ms sequence, the power in the vertical trapping beam  $P_z$  is rapidly increased, as can be seen in Fig. 2(a). This change is likely non-adiabatic for atoms in the wings of the horizontal ODT and the cloud may no longer be in thermal equilibrium. This is likely why the calculated  $\text{PSD}_c$  appears to increase beyond  $\sim 1$  before the appearance of a BEC. Notably this non-adiabatic portion of the sequence occurs only after  $\text{PSD}_c$  has reached 0.4, and thus it does not affect the cooling efficiency estimate of  $\gamma \approx 16$  for the cooling up to  $\text{PSD}_c = 0.1$ .

The peak trap depth  $U_{i,0}$  for each beam was determined from the beam waist  $w_{i,0}$  and radial trap frequency  $\omega_{i,r}$  measured for each beam. The beam waists, defined as the radius at which the intensity falls to  $1/e^2$  of its peak value, were measured by profiling the trap beams on a separate test setup which focused the light outside of the vacuum chamber. The trap frequencies were directly measured by carefully perturbing the position of a cloud in the cODT and observing its oscillations. Before perturbing the cloud, it was first cooled sufficiently to make it well-confined to the central region of the cODT so that the potential was approximately harmonic. The peak trap depth for each beam could then be calculated as  $U_{i,0} = m\omega_{i,r}^2 w_{i,0}^2/4$ . This expression can be derived by equating the spring constant for the trap in the radial direction  $k = d^2U_i(\mathbf{x})/(dr')^2|_{\mathbf{x}=\mathbf{x}_0}$  to its value for a harmonic oscillator  $k = m\omega_{i,r}^2$ .

### COST SCALING

The peak optical depth OD of a pure BEC after sufficient time of flight expansion scales as  $\text{OD} \propto N_{\text{BEC}}/A$  where  $A$  is the area of the cloud in the image. The area scales in proportion to  $\bar{v}^2$  where  $\bar{v}$  is the expansion velocity, which is related to the BEC chemical potential via  $(1/2)m\bar{v}^2 = (2/7)\mu$  in a harmonic trap [35]. Thus  $A \propto \mu$ . Furthermore, the chemical potential for a harmonically-trapped BEC scales as  $\mu \propto N_{\text{BEC}}^{2/5}$  [35], so  $A \propto N_{\text{BEC}}^{2/5}$  and  $\text{OD} \propto N_{\text{BEC}}^{3/5}$ . The expression  $\text{OD}^3 N^{\alpha-9/5}$  then scales as  $(N_{\text{BEC}})^\alpha$ . Notably this scaling also applies to a harmonically-trapped BEC when imaged in situ. There, the BEC radius  $R$  scales as  $R \propto N_{\text{BEC}}^{1/5}$  [35]. In that case,  $A \propto R^2 \propto N_{\text{BEC}}^{2/5}$  as before. The same arguments then apply again, indicating that  $\text{OD}^3 N^{\alpha-9/5}$  scales as  $(N_{\text{BEC}})^\alpha$  for a harmonically-trapped BEC in situ just as it does for a BEC after long time of flight expansion.

The scaling of  $\text{OD}^3 N^{\alpha-9/5}$  for a purely thermal cloud is also of note. For a harmonically-trapped thermal cloud, the RMS size in a given direction for any time of flight is proportional to  $T^{1/2}$ , so  $A \propto T$ . Thus  $\text{OD} \propto N/T$  and  $\text{OD}^3 N^{\alpha-9/5}$  scales in proportion to  $N^{\alpha+(6/5)}/T^3$ . Clouds with smaller temperatures are favored by the cost

function, and clouds with larger atom numbers are favored as long as  $\alpha > -6/5$ . For the case  $\alpha = -1/5$ , the value of  $\text{OD}^3 N^{\alpha-9/5}$  scales in proportion to  $N/T^3$ , which is proportional to  $\text{PSD}_c$ . That choice of  $\alpha$  was often used when optimizing individual stages before reaching the threshold to BEC. However note that this choice of  $\alpha$  leads to the scaling  $\text{OD}^3 N^{\alpha-9/5} \propto N_{\text{BEC}}^{-1/5}$  for a pure BEC and is thus not a good choice when the cloud reaches condensation.

Simply taking the largest optical depth measured in any single pixel of an absorption image as OD makes it prone to noise. In this work, OD was set to the average OD of several pixels with the largest OD to reduce noise.

### RAMAN COOLING LASER

Standard Doppler cooling requires a laser with linewidth narrow compared to the optical transition linewidth in order to achieve optimal temperatures. This places stringent technical requirements for Doppler cooling on narrow optical transitions. By contrast, Raman cooling can achieve similar velocity resolution and associated temperatures with a comparatively broad laser. In this work, the light for the Raman coupling and optical pumping beams, which drive the up-leg and down-leg of the Raman transition respectively, was derived from the same laser. This ensures that any laser frequency noise is common mode between the two legs of the Raman transition and makes it possible to resolve Doppler shifts much smaller than the laser linewidth. A DBR laser diode (Photodigm PH795DBR180TS) without an external cavity was sufficient to generate the Raman cooling light. The forgiving laser linewidth requirements further simplify implementation of our BEC production approach compared to schemes which require Doppler cooling on narrow optical transitions. Thus our approach may be useful even for species which include narrow optical transitions.